Green Chemistry

PAPER

View Article Online
View Journal | View Issue

Check for updates

Cite this: *Green Chem.*, 2023, **25**, 1395

Facile synthesis of SAPO-34 nanocrystallites with excellent performance for the dehydration of carbohydrates to 5-hydroxymethylfurfural†

Pengfei Wu,[a,b] Miao Yang,[b] Jifeng Pang,[a] Dong Fan,[b] Lei Song,[a] Tantan Sun,[c] Mingyuan Zheng,*[a] Peng Tian*[b] and Tao Zhang[a]

Received 15th November 2022,
Accepted 13th January 2023

DOI: 10.1039/d2gc04301g

rsc.li/greenchem

The conversion of biomass resources into 5-hydroxymethylfurfural (5-HMF) is of great significance for the valorization of biomass into key chemicals and fuels. However, designing heterogeneous catalysts with controllable Brønsted and Lewis acid sites for achieving high yields of 5-HMF remains a challenge. Herein, a highly efficient SAPO-34 nanocrystallites catalyst has been synthesized by a facile strategy, employing commercial low-cost organosilane [3-glycidoxypropyltrimethoxysilane (AC-230)] together with seeds and microporous template triethylamine. The complex functionalities of AC-230 were investigated by conditional experiments and systematic characterizations. The resultant SAPO-34 nanocrystallites (SP-MS) have an ultra-high external surface area (180 m^2 g^{-1}), large mesopore volume (0.51 cm^3 g^{-1}), a high amount of accessible Brønsted/Lewis acid, and good hydrophilicity. For the conversion of mono-, di-and poly-saccharides into 5-HMF, SP-MS exhibited remarkable activity. Typically, an 81% yield of 5-HMF with a complete glucose conversion was achieved in a biphasic NaCl–H_2O/methyl isobutyl ketone solvent system at 170 °C within 45 min, obviously better than other heterogeneous acid catalysts. According to the kinetic study, the Lewis acid sites over SP-MS decreased the apparent activation energy (85 kJ mol^{-1}) of glucose isomerization, and then the abundant Brønsted acid sites boosted the 5-HMF yields. More attractively, the catalytic activity can be restored after at least four cycles. This work is anticipated to provide insights into designing efficient and robust SAPO catalysts for 5-HMF production.

1 Introduction

Intensive research on the efficient utilization of biomass resources to produce advanced liquid fuels and chemicals has been underway to address the shortage of fossil fuels and associated environmental issues.[1–3] In particular, attention has been focused on synthesizing high-value-added chemicals from the abundant plant-derived carbohydrates.[4,5] As a versatile furan building block molecule, 5-HMF has been listed as one of the "top-12 value-added biomass-derived platform chemicals" by the U.S. Department of Energy based on the large spectrum of chemical intermediates and end-products that are produced,[6] including furanic bio-polyester monomers such as 2,5-furandicarboxylic acid (FDCA), 2,5-furandimethanol (BHMF) and 2,5-bis(hydroxymethyl)tetrahydrofuran (BHMTHF).[7–10] 5-HMF can be obtained from the conversion of several glucose-derived substrates *via* a tandem route in aqueous solution, which is cooperatively catalyzed by both Brønsted and Lewis acid sites.[11–13] Taking glucose as a typical representative, the reaction network includes two key steps (Scheme 1): isomerization of glucose to fructose facilitated by Lewis acid sites and the dehydration of the obtained fructose

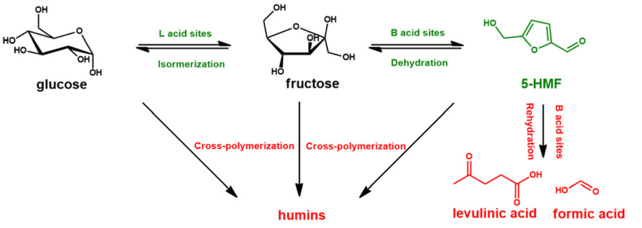

Scheme 1 The proposed reaction pathway for the conversion of glucose into 5-HMF over the acid catalyst.

---

[a] *CAS Key Laboratory of Science and Technology on Applied Catalysis, Dalian Institute of Chemical Physics, Chinese Academy of Sciences, Dalian 116023, China. E-mail: myzheng@dicp.ac.cn*

[b] *National Engineering Laboratory for Methanol to Olefins, Dalian National Laboratory for Clean Energy, Dalian Institute of Chemical Physics, Chinese Academy of Sciences, Dalian 116023, China. E-mail: tianpeng@dicp.ac.cn*

[c] *Key Laboratory of Biomass Chemical Engineering of Ministry of Education, College of Chemical and Biological Engineering, Zhejiang University, Hangzhou 311215, China*

† Electronic supplementary information (ESI) available. See DOI: **https://doi.org/10.1039/d2gc04301g**

on Brønsted acid sites to produce 5-HMF. Nevertheless, strong acid sites simultaneously facilitate undesirable side reactions such as rehydration of 5-HMF to levulinic acid and formic acid as well as cross-polymerization of 5-HMF/intermediates to humins.[5] Given such circumstances, constructing moderate and adequate Lewis/Brønsted acid sites to catalyze the rapid dehydration of carbohydrates toward 5-HMF is crucial for minimizing side reactions and thus achieving a high yield of 5-HMF.

Hitherto, industrial production of 5-HMF, using mineral acids (H_2SO_4 and HCl) as the catalyst, by the dehydration of the costly fructose has been performed. This process is plagued by issues such as equipment corrosion and waste treatment.[14] Owing to the recoverability and low corrosivity of heterogeneous acid catalysts, significant efforts have been made to explore their catalytic application for 5-HMF production, including ion exchange resins,[15] metal oxides,[16] heteropoly acids,[17] graphene oxide,[18] aluminosilicate molecular sieves,[19–22] and silicoaluminophosphate (SAPO) molecular sieves. Among them, SAPO molecular sieves stand out for their ultra-high (hydro)thermal stability, original porosity, tunable acidity, and hydrophilicity.[23,24] Notably, as the most important representative of SAPOs, the small-pore SAPO-34 with 8-membered ring (8-MR) channels and CHA cages exhibits unanticipated catalytic performance in the dehydration of carbohydrates to high-valued platform chemicals. Dhepe *et al.* first disclosed that SAPO-44 (analogue of SAPO-34) showed superior catalytic activity compared with conventional aluminosilicate (beta, MOR and USY) and other SAPO catalysts (SAPO-5, SAPO-11, and SAPO-46) in the conversion of softwood hemicellulose to furfural reaction, and 63% yield of furfural could be achieved in the toluene/H_2O biphasic system.[25] Zhang *et al.* broadened the substrate range by employing SAPO-34 to convert C6 sugars (glucose, fructose, and sucrose) into 5-HMF in the high boiling-point solvent γ-valerolactone.[26] Recently, to adjust the surface acidity of the catalyst, Wang *et al.* modified SAPO-34 with Sn for glucose to 5-HMF reaction and achieved a 98.5% glucose conversion with 64.4% yield of 5-HMF in the biphasic NaCl–H_2O/tetrahydrofuran solvent system.[27] As the kinetic diameter of carbohydrates (*e.g.* glucose: 0.73 nm) and product (5-HMF: 0.62 nm) are obviously larger than the micropore size of SAPO-34 (0.38 nm), the reactions occur primarily on the external acid sites of the catalysts. The narrow 8-MR pore openings of SAPO-34 hinder the diffusion of reactants, which suppresses the intracrystalline side reactions and subsequent coke deposition. On the other hand, the abundant intracrystalline acid sites of the large SAPO-34 crystals are not utilized in the reaction.

Therefore, it would be highly desirable to synthesize highly crystallized nanosized/hierarchical SAPO-34 with large external surface area, since they can provide a large amount of accessible active sites and increased hydrophilicity, both of which facilitate the further improvement of the catalytic performance for 5-HMF productivity.[25,28] Over the past decades, tremendous efforts have been made to develop synthetic strategies for the preparation of nanosized or hierarchical SAPO-34.[29] Unfortunately, it remains a challenge hitherto to synthesize SAPO-34 with ultra-high external surface area (>150 $m^2\ g^{-1}$) while maintaining good crystallinity (Table S1†), especially when using inexpensive organic amine template. Organosilanes have been proved to be the most prominent crystal growth inhibitor to fabricate nanosized SAPO-34 through the formation of the R–Si–O–Al bond between organosiloxane groups and the inorganic framework.[30,31] Various oxygen-rich small molecules, or polymers, such as citric acid,[32] β-cyclodextrin,[33] 1,2,3-hexanetriol,[34] polyoxyethylene lauryl ether[35] and polyethylene glycol[35,36] have also been claimed to interact with the SAPO-34 framework *via* the coordination of lone pair of electrons of oxygen atoms to limit the crystal growth. It is thus envisioned that low-cost organosilanes, which contain both an oxygen-containing group and an organosilane group, may have the potential for the efficient synthesis of high-quality nanosized SAPO-34.

Here, the synthesis of SAPO-34 nanocrystallites with ultra-high external surface area and large mesopore volume was realized under the assistance of AC-230, a commercial low-cost epoxy group-containing organosilane coupling agent that is widely used as an adhesion promoter for epoxy resin, glass fiber, and thermosetting resin.[37] The resultant products were characterized systematically, and the formation mechanism of SAPO-34 nanocrystallites was proposed. The high-silica SAPO-34 nanocrystallites were evaluated for the conversion of a variety of carbohydrates, affording remarkable 5-HMF yields.

2 Experimental

2.1 Synthesis

Chemical reagents. Orthophosphoric acid (H_3PO_4, 85 wt%), tetraethyl orthosilicate (TEOS, 98 wt%), aluminium isopropoxide ($Al(i\text{-}C_3H_7O)_3$, 99 wt%), triethylamine (TEA, 99 wt%), D-glucose (99 wt%), D-fructose (99 wt%), D-(+)-cellobiose (99 wt%), D-(+)-sucrose (99 wt%), soluble starch (99 wt%), NaCl (99.5 wt%) and methyl isobutyl ketone (MIBK, 99 wt%) were purchased from Tianjin Kemiou Chemical Reagent Company. Silica sol (31 wt%) was purchased from Shenyang Chemical Industry Co., Ltd. Pseudoboehmite (72.5 wt%) was purchased from Shandong Aluminum Industry Co., Ltd. 3-Glycidoxypropyltrimethoxysilane ($CH_2OCHCH_2O(CH_2)_3Si(OCH_3)_3$, AC-230, 99 wt%) was purchased from Nanjing Aocheng Chem Co. ZSM-5 (Si/Al = 18), MCM-22 (Si/Al = 15), USY (Si/Al = 8) and beta (Si/Al = 12.5) were purchased from Nankai University Catalyst Co., Ltd. Strong-acid ion exchange resin was purchased from Shanghai Aladdin Biochemical Technology Co., Ltd. All chemicals were used as received without any further purification.

Preparation of milled SAPO-34 seeds. SAPO-34 seeds were prepared according to our previous report.[38]

Synthesis of SP-M*n*. All syntheses were performed using the hydrothermal method. A typical synthesis procedure was as follows: H_3PO_4 and $Al(i\text{-}C_3H_7O)_3$ were first added into deionized water and stirred for 30 min. Then, the organic template TEA, SAPO-34 seeds, TEOS, and AC-230 were added in a sequence. The amount of the seeds was calculated using the following formula: seeds amount (x) = M(milled SAPO-34) × 100 / M(Al_2O_3 + P_2O_5 + SiO_2)$_{gel}$, where milled SAPO-34 and M(Al_2O_3 + P_2O_5 + SiO_2)$_{gel}$ stand for the weights of the milled SAPO-34 and the dry mass of the three inorganic oxides in the starting mixture. The mixture was stirred for 12 h and transferred into a stainless steel autoclave and heated at 200 °C for 24 h under rotation. The autoclave was cooled and the solid product was recovered by filtration, washed three times with deionized water, and dried at 110 °C, overnight. Finally, the product was calcined at 600 °C for 4 h to remove the organic species.

Synthesis of SP-*n*. The synthetic procedure of SP-*n* is the same as SP-M*n* except that SAPO-34 seeds are not added.

Synthesis of conventional SAPO-34 (SP-C). For comparison, a reference sample SP-C with silica content similar to SP-MS was synthesized using silica sol as the Si source and pseudoboehmite as the Al source. The synthesis procedure was the same as SP-*n*.

2.2 Characterization

The powder X-ray diffraction (XRD) patterns were recorded on a PANalytical X′ Pert PRO X-ray diffractometer with Cu-Kα radiation (λ = 1.54059 Å), operating at 40 kV and 40 mA. The crystal morphology was observed by scanning electron microscopy (SEM) using a field emission SEM (Hitachi SU8020). Transmission electron microscopy (TEM) images were recorded with a JEM-2100 electron microscope. Textural properties of the calcined samples were measured by N_2 adsorption at −196 °C on a Micromeritics ASAP 2020 analyzer. The total surface area was calculated based on the Brunauer–Emmett–Teller (BET) equation. The micropore volume and micropore surface area were evaluated using the *t*-plot method. The mesopore volume and mesopore surface area were evaluated from the adsorption isotherm by the Barrett–Joyner–Halenda (BJH) method. The temperature-programmed desorption of ammonia (NH_3-TPD) was carried out using a Micromeritics Autochem II 2920 device. The calcined samples (200 mg) were outgassed in a He flow at 600 °C for 60 min. Then, the samples were cooled to 100 °C and subjected to a flow of NH_3/He for 60 min to saturate the sample with NH_3. Then, the samples were purged with a He flow to remove the weakly adsorbed NH_3 molecules. The measurement of the desorbed NH_3 was performed from 100 °C to 650 °C at a heating rate of 10 °C min^{-1} under a He flow (20 mL min^{-1}). The FTIR spectra were collected on a Bruker Tensor 27 instrument. The calcined samples were dehydrated at 400 °C for 1 h under a vacuum of 1.0×10^{-2} Pa, and the IR spectrum was recorded at room temperature. Thermogravimetric and differential thermal analysis (TG-DTG) were performed on a TA SDTQ600 analyzer at a rate of 10 °C min^{-1} in air. All solid–state nuclear magnetic resonance (NMR) experiments were performed on a Bruker Avance III 600 spectrometer equipped with a 14.1 T wide–bore magnet and a 4 mm MAS probe. The resonance frequencies at this field strength were 150.9, 156.4, 242.9, and 119.2 MHz for ^{13}C, ^{27}Al, ^{31}P, and ^{29}Si, respectively. ^{13}C cross-polarization (CP)/MAS NMR spectra were recorded at a contact time of 3 ms and a recycle delay of 2 s at a spinning rate of 12 kHz. ^{27}Al MAS NMR spectra were recorded using one pulse sequence at a spinning rate of 12 kHz. A total of 200 scans were accumulated with a π/8 pulse width of 0.75 μs and a 2 s recycle delay. Chemical shifts were referenced to $(NH_4)Al(SO_4)_2\cdot 12H_2O$ at −0.4 ppm. ^{31}P MAS NMR spectra were recorded with a π/4 pulse width of 2.25 μs and a 10 s recycle delay. Chemical shifts were referenced to 85% H_3PO_4 at 0 ppm. ^{29}Si CP NMR spectra were measured at a contact time of 3 ms and a recycle delay of 2 s. Chemical shifts were referenced to adamantane for ^{13}C and 4,4-dimethyl-4-silapentane sulfonate sodium salt (DSS) for ^{29}Si. Trimethylphosphine (TMP) adsorbed ^{31}P MAS NMR spectra were collected using a 4 mm H–X–Y triple resonance probe under double resonance mode. TMP-adsorbed ^{31}P MAS NMR spectra were recorded with a π/4 pulse width of 2.3 μs and a 20 s recycle delay at a spinning rate of 12 kHz. Chemical shifts were referenced to 85% H_3PO_4 at 0 ppm. For quantification, samples were weighed and dehydrated at 400 °C under vacuum (<10^{-3} Pa) for over 12 h in a dry quartz tube, and TMP was subsequently introduced into the tube at room temperature. Before NMR measurements, the tube was opened in a glove box under dry argon Ar atmosphere, and further treatment under vacuum at 100 °C was conducted to remove the physical adsorbed TMP. The spectra were resolved using DMfit software with Gaussian–Lorentz line shapes, using $(NH_4)_2HPO_4$ (1.13 ppm) as the quantitative external standard for ^{31}P, respectively. Contact angle measurements (sessile drop in the dynamic mode) were performed at room temperature in a KRUSS DSA100 device using ultrapure water as the test liquid. An inductively coupled plasma optical emission spectrometer (ICP-OES) was carried out using a PerkinElmer ICP-OES 7300DV device.

2.3 Catalytic reaction

The dehydration of carbohydrates to 5-HMF was performed in 100 mL thick-wall glass reaction vials. A biphasic system of a saturated solution of NaCl (NaCl–H_2O) and organic (MIBK) solvents was used. In a typical reaction, 0.1 g calcined catalyst and 0.1 g of carbohydrate were mixed with NaCl–H_2O (2 mL) and MIBK (8 mL) in the reactor. The vials were placed in the preheated oil bath under stirring at 750 rpm. Then, the temperature of the reactor reached the desired value in less than 2 min and a timer was started immediately. After the completion of the reaction, the reactor was quickly cooled in an ice-water bath. The solid catalyst and the reaction mixture were separated by centrifugation. The aqueous and organic layers were separated and filtered through a 0.45 μm filter membrane. The aqueous layer was analyzed by high-performance liquid chromatography (Agilent HPLC 1100) equipped with a Rezox™ ROA-Qrganic Acid H + column, refractive index detector (cell temperature of 45 °C), and 5 mM sulfuric acid aqueous was used as the mobile phase with 0.5 mL min^{-1} flow rate. The organic layer was analyzed using a gas chromatograph (Agilent GC 6890N), equipped with a flame ionization detector (FID) and HP-FFAP column.

$$\text{Carbohydrate conversion (mol\%)} = \left(1 - \frac{\text{(moles of initial carbohydrate} - \text{moles of final carbohydrate(HPLC))}}{\text{moles of initial carbohydrate}}\right) \times 100\%$$

$$\text{5-HMF yield(mol\%)} = \frac{\text{moles of 5-HMF (HPLC + GC)}}{\text{moles of initial carbohydrate}} \times 100\%$$

The spent solid catalyst was washed with deionized water, dried at 110 °C and calcined at 600 °C for the recycling test.

For kinetic analysis, the conversion was achieved at less than 20% by controlling the reaction time and reaction temperature.

3 Results and discussion

3.1 Synthesis and physicochemical properties of SAPO-34 nanocrystallites

SAPO-34 nanocrystallites (SP-MS) were synthesized by using organosilane AC-230 together with 5 wt% seeds and microporous template TEA, with a gel molar composition of 4.5TEA/1.0Al_2O_3/1.0P_2O_5/0.66TEOS/0.66AC-230/100H_2O at 200 °C for 24 h. For comparison, a reference sample (SP-C) with Si content similar to the product was prepared without the addition of AC-230 and seeds. As illustrated in Fig. 1a, the as-synthesized SP-MS shows relatively weak and broadened XRD characteristic peaks of the CHA-type molecular sieve, implying the nanocrystal nature of the SAPO-34 product.[39] The substantial decrease in the crystal size was verified by SEM and TEM results. As can be seen, SP-MS presents the elliptical aggregation morphology with an average particle size of about 120 nm (Fig. 1b). Further magnification revealed that the nanoparticles consisted of ultra-small crystallites of 20 nm (Fig. 1c). Comparatively, SP-C (Fig. S1†) exhibits typical cubic morphology with a large particle size of *ca.* 8 μm, which evidences a pronounced crystal growth inhibition in the AC-230-seeds-TEA synthesis system.

The textural properties of the sample SP-MS were characterized by N_2 adsorption–desorption measurements. As shown in Fig. 1d, the isotherms have steep uptakes near $P/P_0 = 0$ due to the intrinsic microporous structure of SAPO-34. Additionally, as compared to SP-C, the nanosized SP-MS exhibits an obvious hysteresis loop at a higher relative pressure of $P/P_0 > 0.9$, ascribed to the capillary condensation in the mesopores and multilayer adsorption in the void space of the nanoparticles. The wide mesopore size distribution for SP-MS is centered at 37 nm. Notably, SP-MS processes a very large external surface area (180 $m^2\ g^{-1}$) and high mesopore volume (0.51 $cm^3\ g^{-1}$), well consistent with its ultra-small primary crystal size. Moreover, the large micropore surface area of 470 $m^2\ g^{-1}$ and micropore volume of 0.22 $cm^3\ g^{-1}$ indicates its good micropore integrity. It is noted that the synthesis of well-crystallized SAPO-34 with such a high external surface area and mesopore volume is rarely reported for amine template systems.

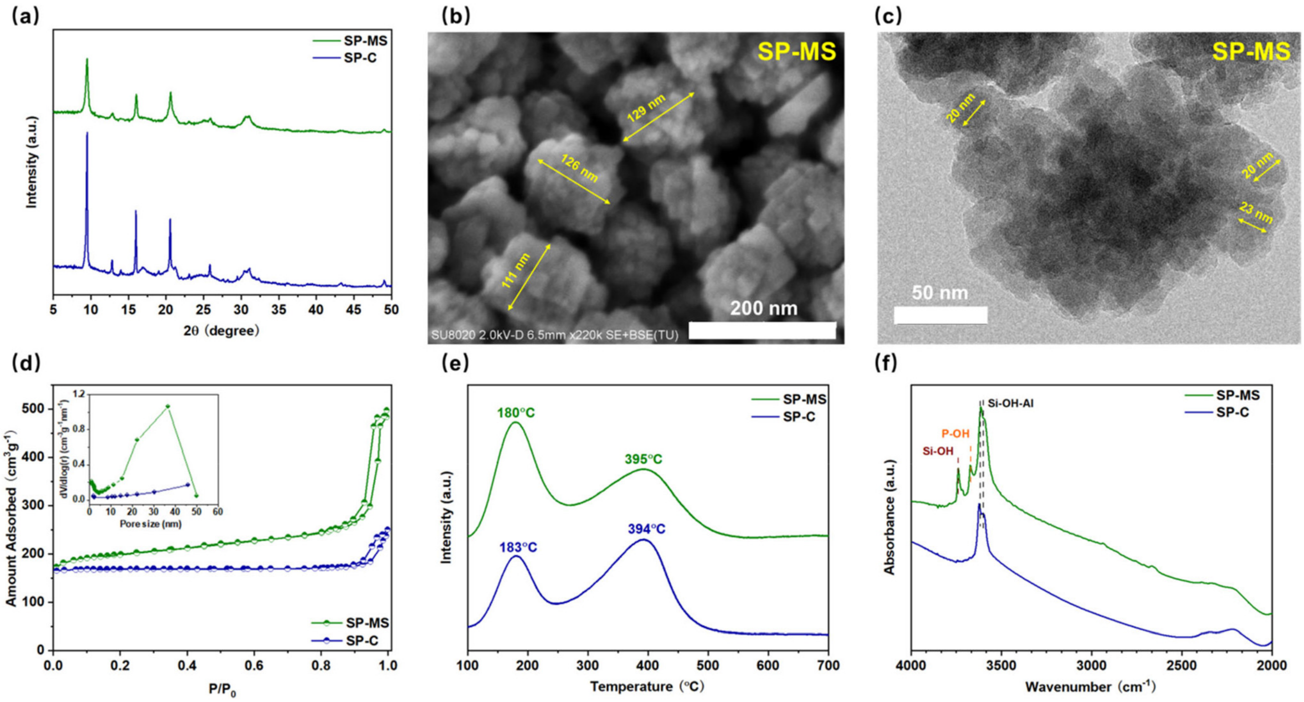

Fig. 1 (a) XRD patterns, (b) SEM image, (c) TEM image, (d) N_2 sorption isotherms (insets show the pore size distributions), (e) NH_3-TPD profiles and (f) FT-IR spectra of SP-MS and SP-C. As-synthesized samples for (a); calcined sample for (b–f).

The acid properties of the samples were investigated by NH_3-TPD and FT-IR. As seen in Fig. 1e, SP-MS, and SP-C have similar acid strength, but SP-MS obviously possesses a higher amount of weak acid sites and a smaller amount of medium/strong acid sites, as compared with SP-C. The FT-IR spectra of the samples (Fig. 1f) give a clear absorption at 3600 and 3625 cm^{-1}, assigned to bridging Si–OH–Al groups (Brønsted acid sites).[40] Moreover, two additional signals at 3741 and 3675 cm^{-1}, originating from Si–OH and P–OH, respectively,[40] can be observed for SP-MS. The results of NH_3-TPD and FT-IR suggest that the addition of AC-230 introduces more defect sites and modifies the acidity of SAPO-34.

3.2 Synthesis parameters and chemical environments of the SAPO-34 crystals

To learn the pivotal parameters affecting the formation of SAPO-34 nanocrystallites, a series of syntheses were carried out based on the gel system of SP-MS. Detailed synthesis conditions and the corresponding results are listed in Table 1. The powder XRD patterns, SEM, and TEM images of the selected samples are presented in Fig. S2† and Fig. 2.

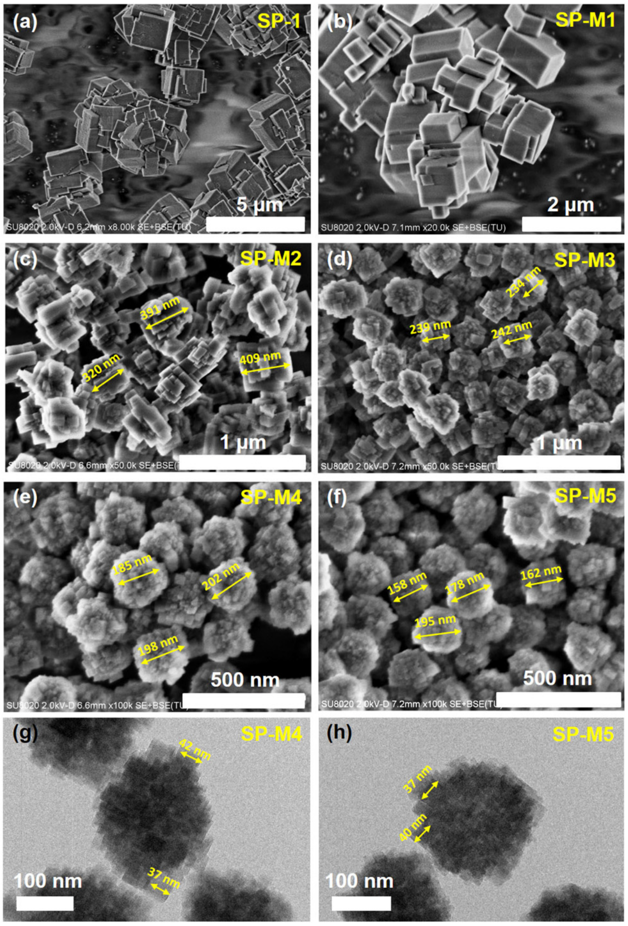

Fig. 2 SEM images of calcined SP-1 (a), SP-M1 (b), SP-M2 (c), SP-M3 (d), SP-M4 (e), SP-M5 (f), and TEM images of calcined SP-M4 (g), SP-M5 (h).

According to the conditional experiment results, the crystallization of the SAPO samples is significantly affected by organosilane AC-230 and seeds. In the absence of AC-230 and seeds, cubic twinned crystals with a particle size of *ca.* 5 µm (SP-1, Fig. 2a) were obtained. When AC-230 was employed as a Si source, either solely or partially with TEOS, it can be seen from Table 1 (SP-2, SP-3, SP-4, and SP-5) that the products became amorphous (Fig. S2a†), even if the crystallization time was fully extended, indicating that simply adding AC-230 into the synthesis system dramatically hinders the crystallization process. Interestingly, with the co-existence of AC-230 and a small amount of seeds, SAPO-34 nanocrystallites could be readily achieved by employing TEOS and AC-230 as Si sources simultaneously. When only 5 wt% seeds were introduced into the gel, the product SP-M1 displayed similar morphology to that of SP-1 with a slightly decreased particle size of 1 µm (Fig. 2b). By increasing the molar ratio of AC-230/Al_2O_3 of the gel from 0.1 to 0.4, while keeping the TEOS/Al_2O_3 ratio constant at 0.4, all samples exhibited broad XRD peaks of SAPO-34

Table 1 Synthesis conditions and resultant products of hydrothermal synthesis

	Gel composition					
Sample	TEOS	AC-230	Seeds	Product phase	Product size	Product composition
SP-MS[a]	0.66	0.66	5%	CHA	120 nm	$Si_{0.173}Al_{0.452}P_{0.375}O_2$
SP-C[b]	—	—	—	CHA	8 µm	$Si_{0.181}Al_{0.450}P_{0.369}O_2$
SP-1[a]	0.4	0	—	CHA	5 µm	$Si_{0.083}Al_{0.524}P_{0.393}O_2$
SP-2[a]	0	0.4	—	Amorphous	—	—
SP-3[a]	0.4	0.1	—	CHA + amorphous	—	—
SP-4[a]	0.4	0.2	—	Amorphous	—	—
SP-5[a,c]	0.4	0.2	—	Amorphous	—	—
SP-M1[a]	0.4	0	5%	CHA	1 µm	$Si_{0.093}Al_{0.520}P_{0.387}O_2$
SP-M2[a]	0.4	0.1	5%	CHA	400 nm	$Si_{0.114}Al_{0.482}P_{0.404}O_2$
SP-M3[a]	0.4	0.2	5%	CHA	250 nm	$Si_{0.123}Al_{0.479}P_{0.398}O_2$
SP-M4[a]	0.4	0.4	5%	CHA	200 nm	$Si_{0.132}Al_{0.472}P_{0.396}O_2$
SP-M5[a]	0.4	0.6	5%	CHA	200 nm	$Si_{0.134}Al_{0.470}P_{0.395}O_2$
SP-M6[a]	0	0.4	5%	AFI + CHA	—	—

[a] Initial gel molar composition: TEA/Al_2O_3/P_2O_5/TEOS/AC-230/H_2O = 4.5/1.0/1.0/x/y/100. [b] For SP-C, pseudoboehmite and silica sol are used as the Al source and Si source, respectively. Initial gel molar composition: TEA/Al_2O_3/P_2O_5/SiO_2/H_2O = 3.5/1.0/0.8/1.0/55. [c] Crystallization time: 96 h.

(Fig. S2b†). SEM images (Fig. 2b–e) reveal that with the increase of AC-230 in the initial gel, the secondary particle sizes of the samples gradually decrease from 1 μm to 200 nm, indicating that the addition of AC-230 can restrain the growth of the crystals under the assistance of seeds. In addition, XRF analysis shows a notable increase in product Si content from SP-M1 to SP-M4, which evidences the incorporation of the organosiloxane group into the framework of SAPO-34. Notably, the chemical composition (Table 1, SP-M5) and morphology (Fig. 2f and h) of the product remain nearly unaltered upon further increasing the AC-230/Al_2O_3 ratio. It is speculated that, in the AC-230-seeds-TEA system, the capability of the organosilane in the framework may have a maximum. Even in the presence of seeds, pure SAPO-34 cannot be synthesized using AC-230 as the only Si source (Table 1, SP-M6). This may be attributed to the bulk oxygen-containing group of the AC-230 molecule, making the organosilane insufficient to construct the CHA structure. In summary, the above experimental results illustrate that the co-existence of TEOS/AC-230 and seeds in the initial gel is crucial for the formation of SAPO-34 nanocrystallites.

N_2 adsorption isotherms and textural properties of the samples are depicted in Fig. S3† and Table 2, respectively. Besides the abrupt inclination at the high-pressure region, there exist hysteresis loops at $0.5 < P/P_0 < 0.75$ for the nano-sized samples, ascribed to the capillary condensation in the mesopores. In comparison with the samples synthesized without the use of AC-230 (SP-1 and SP-M1), an apparently increased external surface area (107–184 $m^2\ g^{-1}$) and mesopore volume (0.25–0.44 $cm^3\ g^{-1}$) from SP-M2 to SP-M5 were achieved with the increased dosage of AC-230.

Table 2 Textural properties of the samples

Sample	Surface area ($m^2\ g^{-1}$)			Pore volume ($cm^3\ g^{-1}$)	
	S_{BET} [a]	S_{micro} [b]	S_{exter} [b]	V_{micro} [b]	V_{meso} [c]
SP-MS	649	470	180	0.22	0.51
SP-C	533	517	15	0.25	0.11
SP-1	549	525	24	0.26	0.07
SP-M1	549	545	4	0.27	0.00
SP-M2	644	537	107	0.26	0.25
SP-M3	630	479	151	0.23	0.35
SP-M4	645	461	184	0.22	0.39
SP-M5	596	420	176	0.21	0.44

[a] Total surface area is determined by the BET equation. [b] Micropore surface area, micropore volume and external surface area are determined by the *t*-plot method. [c] Mesopore volume is determined from the adsorption isotherm by the BJH method.

To investigate the local Si atomic environments and the status of organosilane in the samples, the as-synthesized SP-MS and reference sample SP-C were analyzed by solid-state ^{29}Si and ^{13}C MAS NMR. Both samples exhibited complicated ^{29}Si CP MAS NMR spectra (Fig. 3a), which contain a quintuplet of resonance signals centered at −92, −95, −99, −104, and −109 ppm, arising from tetrahedral $Si(OAl)_n$ (n = 4, 3, 2,1, and 0) species in the SAPO-34 framework.[41] Meanwhile, an additional broad resonance from −47 to −68 ppm attributable to the Tn groups ($Tn = RSi(OAl)_n(OH)_{3-n}$, n = 2 and 3) can be observed for SP-MS, confirming that the organo-siloxane groups of AC-230 have been condensed into the framework.[42] The appearance of organosilane was also evidenced by ^{13}C MAS NMR spectroscopy (Fig. 3b). With the exception of two strong signals at 48 and 9 ppm assigned to the methyl and methylene groups of TEA, respectively, all the remaining weak peaks can be ascribed to the organic groups of AC-230. The organics of the as-synthesized samples were quantitatively analyzed by TG-DTA. As seen in Fig. S4(a) and Table S2,† the organic weight losses rise from 12.6 to 16.9 wt% with the increase of AC-230/Al_2O_3 ratio, which is consistent with the XRF results and confirms the increased incorporation of the organosilane. From Fig. S4(b),† sample SP-M1 just shows one exothermic peak centered at 432 °C in the DTA curve corresponding to the combustion of TEA molecules encapsulated in the CHA cages. The SAPO-34s synthesized with AC-230 exhibit additional exothermic signals at around 312 and 596 °C, ascribed to the thermal decomposition of the organosilane.

The ^{27}Al and ^{31}P MAS NMR spectra of the samples are presented in Fig. S5.† The difference between SP-MS and SP-C is hardly noticeable. The ^{27}Al NMR spectra present a broad dominant signal at 37 ppm together with two weak shoulders at 13 and −12 ppm, attributing to tetra-, penta-, and hexa-coordinated Al species, respectively.[43] The ^{31}P NMR spectra give solitary resonance at −29 ppm due to the tetrahedral PO_4 species. The slightly asymmetrical profile of SP-MS suggests the existence of not fully condensed P species.[43] The detailed deconvolution results are provided in Section 3.4.

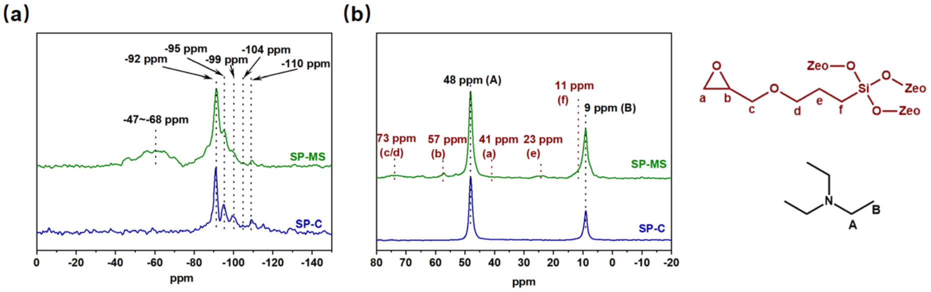

Fig. 3 ^{29}Si CP MAS NMR spectra (a) and ^{13}C MAS NMR spectra (b) of the as-synthesized samples.

3.3 Formation mechanism of SAPO-34 nanocrystallites

On the basis of the above conditional experiments and characterization data, AC-230 played a non-substitutable role in the synthesis of SAPO-34 nanocrystallites. The presence of a small amount of seeds, on the other hand, was also essential since they promoted the formation of crystalline products. A possible crystallization process is therefore proposed and depicted in Scheme 2. Classically, the hydrothermal synthesis of molecular sieves involves two steps: (I) the induction period, which is the process of assembling preliminary building units from supersaturated gels to form the nuclei; (II) the crystal growth period, referring to the rapid polymerization of the nutritive material on the nuclei to form the massively-ordered crystal.[44] Based on the Ostwald ripening mechanism, the smaller crystal nuclei are prone to redissolve during the crystal growth period, which in turn permits the larger crystalline particles to grow even more. Therefore, even though more crystal nuclei are formed in a short time with the assistance of the seeds, the aggregation of crystal nuclei results in a limited change in the product morphology. In addition to three methoxysilane groups, the AC-230 molecule contains an oxygen-containing epoxy group, which strengthens the interactions between the organosilane and the nuclei surface *via* the coordination of the lone pair electrons of oxygen atoms.[33,35,36] Through the hydrolyzed silanol group and epoxy group at both ends of the molecule, the organosilane serves as an immobilization agent to construct a segregated network of crystal nuclei, inhibiting the redissolution and overgrowth of the crystal nuclei and thus resulting in SAPO-34 nanoaggregates. In the absence of the seeds, excessive AC-230 molecules may wrap up the rare crystal nuclei, which severely obstructed the crystal growth to obtain crystalline products.

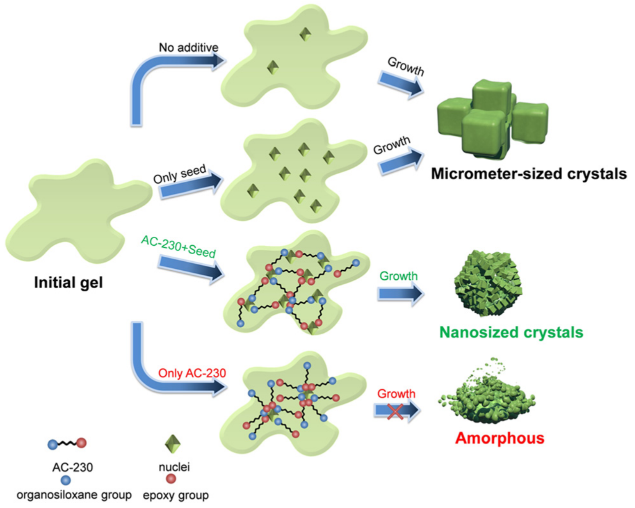

Scheme 2 Proposed crystallization process of the SAPO-34 products. TEA and Si/Al/P species are omitted for clarity.

3.4 Catalytic performance in the dehydration of carbohydrates in 5-HMF

The catalytic performance of SAPO-34 samples was evaluated in biomass-derived carbohydrate dehydration to 5-HMF reaction, and the results are summarized in Table 3. Preliminary experiments were carried out with glucose as the substrate due to its greater availability and lower cost, in a low-boiling H_2O/MIBK biphasic solvent system.[45,46] As expected, the nanosized SP-MS has obviously higher glucose conversion (49.2%) and 5-HMF yield (26.0%) than the reference sample SP-C (33.7% and 5.9%) at 170 °C within 45 min. In addition, SP-MS exhibits higher catalytic activity compared with SP-M3, SP-M4, and SP-M5 (Table 3, entries 4–6), though these samples possess comparable textural properties. This should be owing to the higher Si content of SP-MS, which can provide more active sites for carbohydrate conversion.

Previous reports showed that in the biphasic system, the presence of NaCl increases the partition coefficient ($C_{\text{org.}}/C_{\text{aq.}}$) of 5-HMF.[17,47,48] By means of the "salting-out effect", the produced 5-HMF immediately migrates from the aqueous phase to the stable organic phase, thus promoting the dehydration reaction by shifting the equilibrium towards the formation of 5-HMF and avoiding the side reactions. Therefore, NaCl–H_2O/MIBK solvent system was chosen for further catalytic study.

Table 3 Catalytic performance of samples in the dehydration of carbohydrates into 5-HMF [a]

Entry	Catalyst	Substrate	Solvent[b]	Conversion of substrate (%)	Yield of 5-HMF (%)
1	Blank	Glucose	8 mL MIBK + 2 mL H_2O	9.4	6.3
2	SP-C	Glucose	8 mL MIBK + 2 mL H_2O	33.7	5.9
3	SP-MS	Glucose	8 mL MIBK + 2 mL H_2O	49.2	26.0
4	SP-M3	Glucose	8 mL MIBK + 2 mL H_2O	37.8	14.0
5	SP-M4	Glucose	8 mL MIBK + 2 mL H_2O	42.5	20.8
6	SP-M5	Glucose	8 mL MIBK + 2 mL H_2O	43.7	22.2
7	Blank	Glucose	8 mL MIBK + 2 mL NaCl–H_2O	13.8	2.1
8	SP-C	Glucose	8 mL MIBK + 2 mL NaCl–H_2O	82.1	51.4
9	SP-MS	Glucose	8 mL MIBK + 2 mL NaCl–H_2O	>99	81.3
10	SP-MS	Fructose	8 mL MIBK + 2 mL NaCl–H_2O	>99	84.8
11	SP-MS	Sucrose	8 mL MIBK + 2 mL NaCl–H_2O	>99	70.4
12	SP-MS	Cellobiose	8 mL MIBK + 2 mL NaCl–H_2O	>99	73.4
13	SP-MS	Soluble starch	8 mL MIBK + 2 mL NaCl–H_2O	—	57.1

[a] 0.1 g substrate, 0.1 g catalyst, 10 mL solvent, 170 °C, 45 min. [b] NaCl–H_2O: saturated solution of NaCl.

Results in Table 3, entries 8 and 9 clearly evidence the significant increase in catalytic activity and selectivity for 5-HMF over SAPO-34 catalysts when NaCl was added. Notably, a complete glucose conversion with an 81.5% yield of 5-HMF was achieved over SP-MS under the optimized reaction time (Fig. S6†). Neither levulinic acid nor formic acid was detected in the reaction system, likely owing to the intrinsic medium-strength acidity of SAPO-34, which inhibits the subsequent rehydration of 5-HMF. Moreover, SP-MS is also highly active for the conversion of other mono-, di- and polysaccharides (Table 3, entries 10–13), giving a complete conversion with high 5-HMF yields (57–85%).

For comparison, a variety of heterogeneous acid catalysts were employed to catalyze the conversion of glucose. As depicted in Fig. 4, SP-MS outperformed all commercial aluminosilicate zeolites and strong-acid ion exchange resins, despite their large porosity (Table S3†) and strong acidity (Fig. S7†). One explanation is that in the liquid-phase reaction, MIBK molecules preferentially occupy the channels of the medium-pore (10-MR) and large-pore (12-MR) zeolites to hinder the internal diffusion of glucose, causing low utilization of the intracrystalline acid sites.[45] More seriously, in a hot aqueous solution, the frameworks of aluminosilicate zeolites are more susceptible to severe collapse (especially for MCM-22 and beta, as shown in Fig. S8†) than those of small-pore SAPOs, resulting in the loss of active sites. While for the strong-acid ion exchange resin, the poor catalytic activity should stem from the absence of Lewis acid sites and inferior thermal stability.

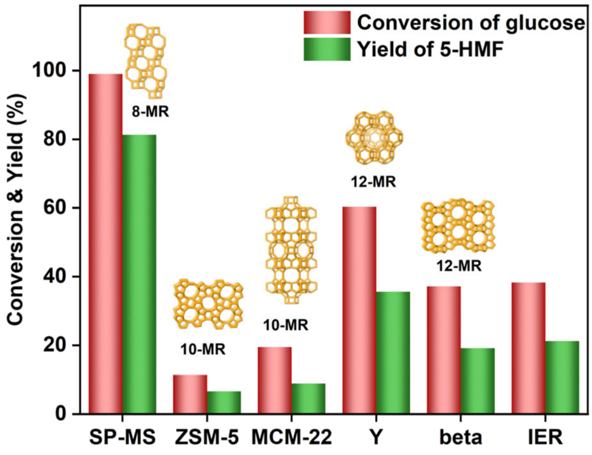

Fig. 4 Glucose conversion and 5-HMF yield in the dehydration of glucose reaction over heterogeneous acid-catalysts. IER: strong-acid ion exchange resin. Reaction condition: 0.1 g glucose, 0.1 g catalyst, 2 mL NaCl–H_2O + 8 mL MIBK, 170 °C, 45 min.

As the carbohydrates have obviously larger kinetic diameters than the micropore size of SAPO-34 (3.8 Å), the catalytic performance is believed to be strongly correlated with the physicochemical properties of the external surface of SAPO-34 crystals. By using the bulky guest molecule TMP (5.5 Å) as the adsorbent, the corresponding ^{31}P MAS NMR spectra were measured, which can quantify the acid types distributed on the external surface and their relative amounts, as well as reveal the chemical environments of the SAPO framework atoms.[49] According to the deconvolution analysis of the spectrum of SP-MS (Fig. 5a), there are two types of framework P atoms, including P–OH (−25 ppm) and predominant PO_4 species (−29 ppm), in agreement with the FT-IR results. Additionally, two resonance signals at −5 and −46 ppm, attributed to TMP chemisorbed on Brønsted and Lewis acid sites of the external surface, respectively, can be identified. The corresponding acid densities were calculated to be 0.954 mmol g^{-1} and 0.317 mmol g^{-1}, respectively.[49,50] The considerable proportion of Lewis acid sites might arise from the unsaturated Al species coordinated with the Si–OH generated by the calcination decomposition of the organosilane.[40] Comparatively, the conventional SP-C is deficient in external Brønsted and Lewis acid sites, and framework defects (Fig. 5b). On the other hand, the hydrophilicity of the catalyst has been recognized to play a vital role in determining the distribution of the catalyst between the aqueous and organic phases.[25] As seen in Fig. 5c and d, the nanosized SP-MS is more hydrophilic than SP-C due to its abundant terminal hydroxyl groups. This is beneficial for the adsorption of water-soluble carbohydrates while avoiding secondary reactions of 5-HMF dispersed in the organic phase.[51] Therefore, the superior catalytic performance of SP-MS for carbohydrates dehydration should arise from its larger amount of acid sites on the external surface and better hydrophilicity.

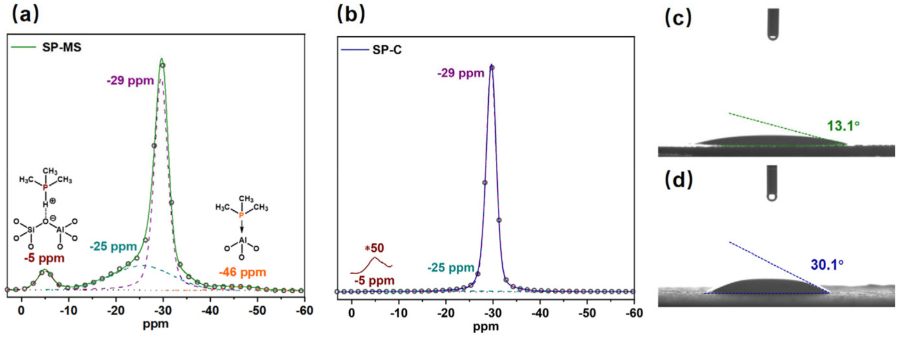

Fig. 5 TMP adsorbed ^{31}P MAS NMR spectra of SP-MS (a) and SP-C (b). Water contact angle measurements of SP-MS (c) and SP-C (d).

3.5 Kinetic studies

To obtain further insight into the intrinsic catalytic performance of SP-MS and SP-C, kinetic studies of glucose and fructose conversion were carried out. Generally, the hydrolysis or dehydration of biomass is assumed to be a first-or second-order reaction.[52,53] Herein, we assumed that the rate for reaching adsorption equilibrium is much faster than that of the reactions, and the obtained experimental data shown in Fig. S9† fit well with the first-order reaction rate equation. Based on the linear Arrhenius plots (Fig. 6), the corresponding apparent activation energy (E_a), pre-exponential factor, and rate constants at a reference temperature (140 °C) are summarized in Table 4. It can be seen from the reaction network (Scheme 1) that carbohydrate substrates and products are inevitably converted to humins. Therefore, increasing reaction rates in the metastable aqueous phase is decisive to obtain a high yield of 5-HMF. SP-MS shows faster reaction rates than SP-C in both glucose isomerization and fructose dehydration, coinciding with its higher external Brønsted and Lewis acid amount. Since the stable pyran ring structure of glucose, the glucose isomerization step usually controls the overall rate of the tandem reactions.[54] This is also the exact case for SP-MS and SP-C, as evidenced by the lower rate constant of glucose isomerization than that of the subsequent fructose dehydration.

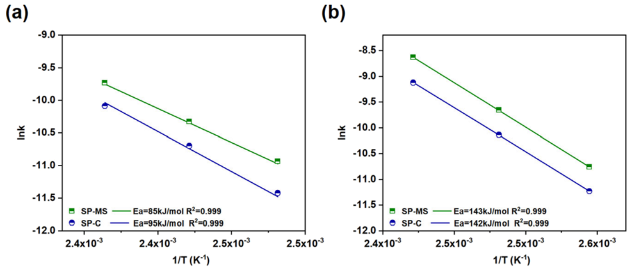

Fig. 6 Arrhenius plots for the conversion of glucose (a) and fructose(b). Reaction condition: 0.1 g substrate, 2 mL saturated solution of NaCl + 8 mL MIBK, 0.1 g catalyst for glucose conversion, 0.02 g catalyst for fructose conversion.

Table 4 Kinetic parameter values for the reaction rates over SP-MS and SP-C

Substrate	Catalyst	E_a(kJ mol^{-1})	$\ln A_0$	$\ln(k_{140\ °C})$	Activity[a]
Glucose	SP-MS	85	14.50	−10.31	1.99×10^{-3}
Glucose	SP-C	95	16.80	−10.70	1.35×10^{-3}
Fructose	SP-MS	143	33.12	−8.63	1.07×10^{-2}
Fructose	SP-C	142	32.27	−9.12	6.52×10^{-3}

[a] Defined as (g of converted carbohydrate)/(g of catalyst)/(reaction time, min) at 140 °C.

In addition, SP-MS shows a lower E_a for glucose isomerization than SP-C (85 kJ mol^{-1} *vs.* 95 kJ mol^{-1}). The value is comparable to that of the classical Lewis acid catalyst Sn-Beta (88 kJ mol^{-1}).[12] This evidences the superiority of SAPO-34 nanoaggregates, which provide accessible active Lewis acid sites to reduce the reaction barrier without requiring extra metal components. By contrast, both catalysts exhibit very close E_a values of 142–143 kJ mol^{-1} for fructose dehydration, implying their identical active sites for the reaction. Of course, there is no doubt that the SP-MS could provide more accessible Brønsted acid sites than SP-C to accelerate the fructose conversion.

3.6 Reusability of the catalyst

Good reusability of the catalyst is of practical significance for reducing production costs. Therefore, regeneration of the SP-MS was evaluated for glucose conversion. Prior to the next run, the recovered catalyst was washed with deionized water and calcined at 600 °C to remove residual organic moieties deposited on the catalyst. As displayed in Fig. 7a, SP-MS maintains a high conversion of glucose during the 4 recycles. The 5-HMF yield shows a decrease after the first run, which, however, reaches steady values of 64–68% in the subsequent runs. After the reactions, there is no obvious framework collapse or dissolution of the nanoaggregates, as evidenced by XRD (Fig. 7b) and TEM (Fig. 7c) analysis. Given that ion-exchange of H-type molecular sieves with Na^+ can improve their hydrothermal stability,[55,56] it is supposed that during calcination treatment, the Na^+ ions remaining on the spent catalyst migrate to the interior of crystals and stabilize the host framework, which can account for the decrease of 5-HMF yield after the first run and the good reproducibility in subsequent

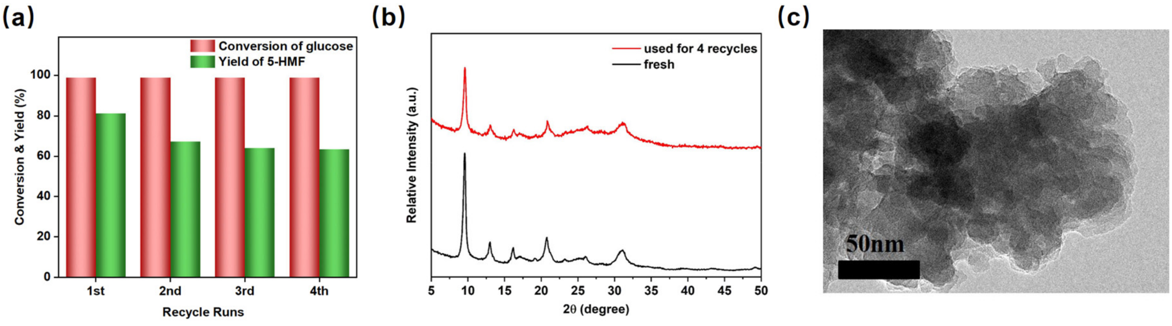

Fig. 7 (a) Recycle reaction results of SP-MS. XRD patterns (b) and TEM image (c) of the used SP-MS after four recycles.

runs. This speculation is well supported by composition analysis, as the fresh catalyst (ICP-OES result: $Si_{0.16}Al_{0.47}P_{0.37}O_2$) underwent an obvious increase in Na content after the first run ($0.14Na_2O{\cdot}Si_{0.15}Al_{0.47}P_{0.38}O_2$), but it remained unchanged afterwards (after 4th: $0.16Na_2O{\cdot}Si_{0.15}Al_{0.48}P_{0.37}O_2$). These results evidence the good stability of SP-MS for glucose conversion, even in a hot aqueous solution with high salt content.

4 Conclusions

Highly efficient SAPO-34 nanocrystallites catalysts with ultrahigh external surface area and large mesopore volume for carbohydrates dehydration to 5-HMF were synthesized by utilizing commercial organosilane AC-230 in the TEA template system. When mono-, di- and polysaccharides were used as substrates, separately, complete conversion was realized together with a high yield of 5-HMF (57–85%). The characterization results and kinetic analysis revealed that the combined contribution of the unique CHA structure, moderate acid strength, abundant accessible Brønsted and Lewis acid sites, and the hydrophilic surface of the catalyst, leads to its excellent catalytic performance. Moreover, the catalyst presented good stability after four reaction cycles. It is envisaged that such a nontoxic, robust and active nanosized SAPO-34 catalyst will hold great potential for high-value utilization of biomass.

Author contributions

The manuscript was completed through the contributions of all authors. All the authors have approved the final version of the manuscript. Pengfei Wu carried out the experiments and wrote the draft. Miao Yang and Jifeng Pang took part in some of the experiment designs and modified the manuscript. Dong Fan carried out the FT-IR measurement. Lei Song drew parts of the scheme. Tantan Sun carried out the TMP adsorbed ^{31}P MAS NMR test. Mingyuan Zheng and Peng Tian guided the research project. Tao Zhang funded and guided the research project.

Conflicts of interest

There are no conflicts to declare.

Acknowledgements

The authors acknowledge the National Natural Science Foundation of China (No. 22108274, 21991090, 21991091, 22171259 and 52276191), the Strategic Priority Research Program of the Chinese Academy of Sciences (Grant No. XDA 21060200), and the Key Research Program of Frontier Sciences, Chinese Academy of Sciences (Grant No. QYZDBSSW-JSC040).

References

1 E. Peeters, S. Calderon-Ardila, I. Hermans, M. Dusselier and B. F. Sels, *ACS Catal.*, 2022, **12**, 9559–9569.
2 W. Luo, W. Cao, P. C. A. Bruijnincx, L. Lin, A. Wang and T. Zhang, *Green Chem.*, 2019, **21**, 3744–3768.
3 Y. Jing, Y. Guo, Q. Xia, X. Liu and Y. Wang, *Chem*, 2019, **5**, 2520–2546.
4 I. Delidovich and R. Palkovits, *ChemSusChem*, 2016, **9**, 547–561.
5 Q. Hou, X. Qi, M. Zhen, H. Qian, Y. Nie, C. Bai, S. Zhang, X. Bai and M. Ju, *Green Chem.*, 2021, **23**, 119–231.
6 T. Xia, W. Gong, Y. Chen, M. Duan, J. Ma, X. Cui, Y. Dai, C. Gao and Y. Xiong, *Angew. Chem., Int. Ed.*, 2022, **61**, e202204225.
7 B. You, X. Liu, N. Jiang and Y. Sun, *J. Am. Chem. Soc.*, 2016, **138**, 13639–13646.
8 K. Vikanova, E. Redina, G. Kapustin, M. Chernova, O. Tkachenko, V. Nissenbaum and L. Kustov, *ACS Sustainable Chem. Eng.*, 2021, **9**, 1161–1171.
9 M. G. Davidson, S. Elgie, S. Parsons and T. J. Young, *Green Chem.*, 2021, **23**, 3154–3171.
10 A. F. Sousa, R. Patrício, Z. Terzopoulou, D. N. Bikiaris, T. Stern, J. Wenger, K. Loos, N. Lotti, V. Siracusa, A. Szymczyk, S. Paszkiewicz, K. S. Triantafyllidis, A. Zamboulis, M. S. Nikolic, P. Spasojevic, S. Thiyagarajan, D. S. van Es and N. Guigo, *Green Chem.*, 2021, **23**, 8795–8820.
11 V. Choudhary, S. H. Mushrif, C. Ho, A. Anderko, V. Nikolakis, N. S. Marinkovic, A. I. Frenkel, S. I. Sandler and D. G. Vlachos, *J. Am. Chem. Soc.*, 2013, **135**, 3997–4006.
12 R. Bermejo-Deval, R. S. Assary, E. Nikolla, M. Moliner, Y. Roman-Leshkov, S. J. Hwang, A. Palsdottir, D. Silverman, R. F. Lobo, L. A. Curtiss and M. E. Davis, *Proc. Natl. Acad. Sci. U. S. A.*, 2012, **109**, 9727–9732.
13 L. Xu, X. Lyu, Y. Jiang, X. Wei, R. Nie and X. Lu, *Green Chem.*, 2022, **24**, 4935–4940.
14 K. I. Galkin and V. P. Ananikov, *ChemSusChem*, 2019, **12**, 2976–2982.
15 M. Ohara, A. Takagaki, S. Nishimura and K. Ebitani, *Appl. Catal., A*, 2010, **383**, 149–155.
16 J. Guo, S. Zhu, Y. Cen, Z. Qin, J. Wang and W. Fan, *Appl. Catal., B*, 2017, **200**, 611–619.
17 G. Qiu, C. Huang, X. Sun and B. Chen, *Green Chem.*, 2019, **21**, 3930–3939.
18 M. Park, J. Lee and B. S. Kim, *Nanoscale*, 2021, **13**, 10143–10151.
19 M. Moreno-Recio, J. Santamaría-González and P. Maireles-Torres, *Chem. Eng. J.*, 2016, **303**, 22–30.
20 V. Rac, V. Rakić, D. Stošić, O. Otman and A. Auroux, *Microporous Mesoporous Mater.*, 2014, **194**, 126–134.
21 J. Wang, Z. Tan, C. Zhu, G. Miao, L. Kong and Y. Sun, *Green Chem.*, 2016, **18**, 452–460.
22 H.-K. Min, S. Kweon, S. Oh, H. An, Y. Cho, H. Min, D. Jo, J. F. Kim, C.-H. Shin, S. B. Kang and M. B. Park, *Green Chem.*, 2021, **23**, 9489–9501.

23 J. Zhong, J. Han, Y. Wei and Z. Liu, *J. Catal.*, 2021, **396**, 23–31.

24 G. K. Beh, C. T. Wang, K. Kim, J. Qu, J. Cairney, Y. H. Ng, A. K. An, R. Ryoo, A. Urakawa and W. Y. Teoh, *Green Chem.*, 2020, **22**, 688–698.

25 P. Bhaumik and P. L. Dhepe, *ACS Catal.*, 2013, **3**, 2299–2303.

26 L. Zhang, G. Xi, Z. Chen, Z. Qi and X. Wang, *Chem. Eng. J.*, 2017, **307**, 877–883.

27 X. Song, J. Yue, Y. Zhu, C. Wen, L. Chen, Q. Liu, L. Ma and C. Wang, *Ind. Eng. Chem. Res.*, 2021, **60**, 5838–5851.

28 P. Bhaumik and P. L. Dhepe, *RSC Adv.*, 2013, **3**, 17156–17165.

29 M. Yang, D. Fan, Y. Wei, P. Tian and Z. Liu, *Adv. Mater.*, 2019, **31**, 1902181–1902195.

30 P. Wu, M. Yang, W. Zhang, S. Xu, P. Guo, P. Tian and Z. Liu, *Chem. Commun.*, 2017, **53**, 4985–4988.

31 C. Sun, A. Zhao, Y. Wang, Z. Wang, J. Zhao, T. Zhao, W. Liu, M. Shi, J. Lu, S. Wu and L. Bu, *Microporous Mesoporous Mater.*, 2021, **310**, 110619–110627.

32 X. Liu, T. Wang, C. Wang, H. Shi, P. Zhang, X. Li, Z. Wang, Z. Yao and M. Hu, *Chem. Eng. J.*, 2020, **381**, 122759–122767.

33 C. Zhang, X. Lu and T. Wang, *J. Energy Chem.*, 2015, **24**, 401–406.

34 J. Zheng, W. Zhang, Z. Liu, Q. Huo, K. Zhu, X. Zhou and W. Yuan, *Microporous Mesoporous Mater.*, 2016, **225**, 74–87.

35 S. R. Venna and M. A. Carreon, *J. Phys. Chem. B*, 2008, **112**, 16261–16265.

36 Q. Sun, N. Wang, G. Guo, X. Chen and J. Yu, *J. Mater. Chem. A*, 2015, **3**, 19783–19789.

37 J. Lu, P. Askeland and L. T. Drzal, *Polymer*, 2008, **49**, 1285–1296.

38 M. Yang, P. Tian, C. Wang, Y. Yuan, Y. Yang, S. Xu, Y. He and Z. Liu, *Chem. Commun.*, 2014, **50**, 1845–1847.

39 P. Wu, M. Yang, L. Sun, S. Zeng, S. Xu, P. Tian and Z. Liu, *Chem. Commun.*, 2018, **54**, 11160–11163.

40 F. D. P. Mees, P. V. Der Voort, P. Cool, L. R. M. Martens, M. J. G. Janssen, A. A. Verberckmoes, G. J. Kennedy, R. B. Hall, K. Wang and E. F. Vansant, *J. Phys. Chem. B*, 2003, **107**, 3161–3167.

41 P. Wu, M. Yang, W. Zhang, S. Zeng, M. Gao, S. Xu, P. Tian and Z. Liu, *Chin. J. Catal.*, 2018, **39**, 1511–1519.

42 C. Wang, M. Yang, P. Tian, S. T. Xu, Y. Yang, D. H. Wang, Y. Y. Yuan and Z. M. Liu, *J. Mater. Chem. A*, 2015, **3**, 5608–5616.

43 J. Han, G. Yang, Y. Zou, X. Chen and V. Valtchev, *Adv. Mater. Interfaces*, 2021, **8**, 2002029–2002037.

44 L. Tosheva and V. P. Valtchev, *Chem. Mater.*, 2005, **17**, 2494–2513.

45 V. V. Ordomsky, J. van der Schaaf, J. C. Schouten and T. A. Nijhuis, *J. Catal.*, 2012, **287**, 68–75.

46 Y. Roman-Leshkov, J. N. Chheda and J. A. Dumesic, *Science*, 2006, **312**, 1933–1937.

47 Y. Roman-Leshkov, C. J. Barrett, Z. Y. Liu and J. A. Dumesic, *Nature*, 2007, **447**, 982–985.

48 N. Candu, M. El Fergani, M. Verziu, B. Cojocaru, B. Jurca, N. Apostol, C. Teodorescu, V. I. Parvulescu and S. M. Coman, *Catal. Today*, 2019, **325**, 109–116.

49 T. Sun, S. Xu, D. Xiao, Z. Liu, G. Li, A. Zheng, W. Liu, Z. Xu, Y. Cao, Q. Guo, N. Wang, Y. Wei and Z. Liu, *Angew. Chem., Int. Ed.*, 2020, **59**, 20672–20681.

50 A. Buchholz, W. Wang, M. Xu, A. Arnold and M. Hunger, *Microporous Mesoporous Mater.*, 2002, **56**, 267–278.

51 J. S. Kruger, V. Nikolakis and D. G. Vlachos, *Curr. Opin. Chem. Eng.*, 2012, **1**, 312–320.

52 J. Wang, J. Ren, X. Liu, G. Lu and Y. Wang, *AlChE J.*, 2013, **59**, 2558–2566.

53 J. Wang, H. Cui, J. Wang, Z. Li, M. Wang and W. Yi, *Chem. Eng. J.*, 2021, **415**, 128922–128931.

54 T. D. Swift, H. Nguyen, Z. Erdman, J. S. Kruger, V. Nikolakis and D. G. Vlachos, *J. Catal.*, 2016, **333**, 149–161.

55 X.-w. Cheng, Y. Zhong, J. Wang, J. Guo, Q. Huang and Y.-c. Long, *Microporous Mesoporous Mater.*, 2005, **83**, 233–243.

56 Z. Zhao, R. Yu, R. Zhao, C. Shi, H. Gies, F.-S. Xiao, D. De Vos, T. Yokoi, X. Bao, U. Kolb, M. Feyen, R. McGuire, S. Maurer, A. Moini, U. Müller and W. Zhang, *Appl. Catal., B*, 2017, **217**, 421–428.